



UNIVERSITY OF LEEDS

This is a repository copy of *Understanding amorphous silica scaling under well-constrained conditions inside geothermal pipelines*.

White Rose Research Online URL for this paper:
<http://eprints.whiterose.ac.uk/135296/>

Version: Accepted Version

Article:

van den Heuvel, DB, Gunnlaugsson, E, Gunnarsson, I et al. (3 more authors) (2018) Understanding amorphous silica scaling under well-constrained conditions inside geothermal pipelines. *Geothermics*, 76. pp. 231-241. ISSN 0375-6505

<https://doi.org/10.1016/j.geothermics.2018.07.006>

© 2018 Elsevier Ltd. Licensed under the Creative Commons Attribution-Non Commercial No Derivatives 4.0 International License (<https://creativecommons.org/licenses/by-nc-nd/4.0/>).

Reuse

This article is distributed under the terms of the Creative Commons Attribution-NonCommercial-NoDerivs (CC BY-NC-ND) licence. This licence only allows you to download this work and share it with others as long as you credit the authors, but you can't change the article in any way or use it commercially. More information and the full terms of the licence here: <https://creativecommons.org/licenses/>

Takedown

If you consider content in White Rose Research Online to be in breach of UK law, please notify us by emailing eprints@whiterose.ac.uk including the URL of the record and the reason for the withdrawal request.



eprints@whiterose.ac.uk
<https://eprints.whiterose.ac.uk/>

1 **Understanding amorphous silica scaling under well-constrained conditions inside geo-**
2 **thermal pipelines**

3

4 Daniela B. van den Heuvel^{a,*}, Einar Gunnlaugsson^b, Ingvi Gunnarsson^b, Tomasz M. Stawski^{a,c},
5 Caroline L. Peacock^a, Liane G. Benning^{a,c,d}

6

7 ^aCohen Geochemistry Group, School of Earth and Environment, University of Leeds, Leeds LS2 9JT, UK

8 ^bReykjavik Energy, Bæjarhals 1, 110 Reykjavik, Iceland

9 ^cGerman Research Center for Geosciences, GFZ, 14473 Potsdam, Germany

10 ^dDepartment of Earth Sciences, Free University of Berlin, 12249 Berlin, German

11

12 *corresponding author: daniela.vandenheuvel@geo.unibe.ch; current address: Rock-Water Interaction Group, In-
13 stitute of Geological Sciences, University of Bern, 3012 Bern, Switzerland

14

15

16 **Keywords:** Silica, geothermal energy, precipitation, mineral scaling, silica sinter

17

18 **Abstract**

19 Amorphous silica is a common precipitate in modern and ancient hot springs and in geothermal
20 power plants, yet the corresponding precipitation rates and mechanisms are still highly debated,
21 primarily due to the plethora of parameters that can affect the reactions in natural waters. Here,
22 we report the results from a first ever industrial-scale time-resolved (1 day to 10 weeks) study
23 of silica precipitation conducted at the Hellisheiði geothermal power plant (SW-Iceland). We
24 show that such in-work pipelines of a geothermal power plant are ideal environments to inves-
25 tigate silica precipitation because the physicochemical conditions are well constrained and con-

stantly monitored. Our results document that amorphous silica forms via two distinct precipitation modes: (1) the fast deposition of continuous botryoidal silica layers and (2) the growth of 3D fan- or ridge-shaped silica aggregates. The continuous layers grow by heterogeneous nucleation and subsequent surface controlled growth by monomer addition. In contrary, the 3D aggregates form through homogeneous nucleation of silica nano- and microparticles in solution, followed by deposition and cementation on the surface of the botryoidal layer. From the time-resolved data, silica precipitation rates of over $1 \text{ g m}^{-2} \text{ day}^{-1}$ are derived. Over time, this deposition of silica on pipelines and fluid handling equipment is detrimental to geothermal power production. Our data does not only help improve our understanding of silica precipitation from geothermal fluids, but the determined silica precipitation mechanisms and rates help improve mitigation strategies against silica scaling inside in-work geothermal power plants.

37

38 **1. Introduction**

Silica (SiO_2) is the most common chemical compound in the Earth's crust and a major component in most geothermal reservoirs. The maximum concentration of silica in geothermal fluids depends on the reservoir temperature and is controlled by quartz solubility or, if the temperature is below $110 \text{ }^\circ\text{C}$, by the solubility of chalcedony (Arnórsson, 1975; Fournier and Rowe, 1966). When these geothermal fluids rise through the crust and emerge at the Earth's surface, rapid cooling results in supersaturation with respect to amorphous silica and precipitation. This sinter formation was studied in numerous modern and ancient terrestrial settings (Braunstein and Lowe, 2001; Cady and Farmer, 1996; Handley et al., 2005; Jones and Renaut, 2004; Konhauser et al., 2004; Konhauser et al., 2001; Mountain et al., 2003; Tobler et al., 2008) and recently, evidence for ancient silica sinter formation has even been documented on Mars (Preston et al., 2008).

50 Identical to their natural analogues, amorphous silica precipitation also occurs in geo-
51 thermal power plants, where fluids are rapidly cooled during energy production, resulting in
52 precipitation of amorphous silica. This so called “silica scaling” is common in high-enthalpy
53 geothermal power plants around the world e.g. Iceland, New Zealand, Japan, the USA, the
54 Lesser Antilles and El Salvador (Dixit et al., 2016; Gunnarsson and Arnórsson, 2003, 2005;
55 Harrar et al., 1982; Meier et al., 2014; Mroczek et al., 2017; Padilla et al., 2005; Rothbaum et
56 al., 1979; Yokoyama et al., 1993). In such systems, amorphous silica precipitation occurs in
57 fluids characterized by a wide range of total silica concentrations (250 to 900 mg/L), tempera-
58 tures (20 to 200 °C), pH (7.2 to 10.2), total dissolved solid concentrations (1300 to
59 93’000 mg/L) and different types of geothermal power plants (e.g. flash steam and binary).
60 Because of the ubiquity and importance of this natural process to renewable energy production
61 and sinter formation, amorphous silica precipitation was studied extensively in the laboratory.
62 Amorphous silica forms via the condensation of silica monomers (H_4SiO_4) into Si-O-Si bonds
63 (Iler, 1979), through polymerisation that can either occur at an interface (e.g., minerals, bacteria
64 or plant matter) where it is described as “heterogeneous nucleation” or in the bulk fluid (“ho-
65 mogeneous nucleation”) (Benning and Waychunas, 2007). In both cases, once silica nuclei
66 have reached a critical size (< 0.5 to 2 nm, Iler, 1979; Noguera et al., 2015; Tobler et al., 2009),
67 they grow spontaneously by the addition of silica from solution. Monomers are the dominant
68 growth species (Bohlmann et al., 1976; Bremere et al., 2000; Mroczek and McDowell, 1988)
69 due to their predominantly neutral charge ($K_a \sim 10^{-8.8}$ at 120 °C) (Fleming and Crerar, 1982;
70 Seward, 1974) in the slightly alkaline pH regime of silica-rich geothermal waters. In contrast,
71 silica polymers and nuclei have a higher dissociation constant ($K_a > 10^{-8}$) (Dugger et al., 1964;
72 Hair and Hertl, 1970), resulting in an overall negative surface charge. Their attachment to ex-
73 isting silica particles or surfaces and the aggregation of silica particles in solution in the absence
74 of bridging cations will thus be limited by electrostatic repulsion. Experimental evidence

75 showed that silica polymerisation, nucleation and growth are enhanced at slightly alkaline pH,
76 elevated temperature, medium to high ionic strength (especially the presence of Al and Fe) and
77 high total silica concentrations (Alexander et al., 1954; Crerar et al., 1981; Fleming, 1986;
78 Gallup, 1997; Goto, 1956; Gunnarsson and Arnórsson, 2005; Icopini et al., 2005; Iler, 1979;
79 Kitahara, 1960; Tobler and Benning, 2013; Weres et al., 1981).

80 These physicochemical factors also affect amorphous silica precipitation from naturally
81 occurring geothermal fluids, where they are in competition with one another and it is often
82 difficult to isolate the dominant parameter in any given fluid. In addition, microbial activity in
83 hot springs (Mountain et al., 2003; Tobler et al., 2008) and high flow rates in geothermal power
84 plants (Meier et al., 2014) make the understanding of these systems highly challenging. There-
85 fore, most laboratory findings cannot be directly transferred and applied to silica precipitation
86 from natural geothermal fluids (Carroll et al., 1998) and although a number of field studies
87 investigating silica sinter formation around hot springs (e.g. Braunstein and Lowe, 2001;
88 Handley et al., 2005; Jones and Renaut, 2004; Konhauser et al., 2004; Mountain et al., 2003;
89 Tobler et al., 2008) give insights into what happens once geothermal solutions reach the Earth
90 surface, they do not address processes that govern formation of amorphous silica inside geo-
91 thermal power plants. This is despite the fact that in-production geothermal power plants rep-
92 resent systems with very well constrained physicochemical conditions that are thus ideal sites
93 to investigate silica precipitation. Such studies would not just help quantify real world silica
94 precipitation but would also inform silica scaling mitigation strategies, thus improving effi-
95 ciency of geothermal energy production and reduce costs.

96 The main reason for the dearth of on-site studies lies in the difficulties in accessing both
97 fluids and silica scales during energy production, without affecting normal operations. A few
98 studies aimed to circumvent these problems by conducting experiments in bypass systems from
99 the main production (Carroll et al., 1998; Dixit et al., 2016; Harrar et al., 1982; Mroczek et al.,

100 2017; Rothbaum et al., 1979). However, the conditions in such bypass systems are most often
101 markedly different from inside in-work pipelines and the bypass is often less well constrained,
102 resulting in data that are only partly applicable to the in-production systems.

103 To change this landscape, we have for the first time conducted a detailed study inside
104 actual in-work geothermal pipelines of a high enthalpy geothermal power plant at Hellisheiði,
105 SW-Iceland. We monitored silica precipitation for up to 10 weeks using stainless steel scaling
106 plates deployed at different positions within the pipelines and characterized the precipitated
107 solids, as well as fluid composition and the physicochemical conditions, under which precipi-
108 tation occurred. Our results reveal that two largely independent pathways control silica precipi-
109 tation. We observe the formation of a continuous, botryoidal layer of silica on the scaling plate
110 surfaces and the growth of 3D structures consisting of silica particles that nucleate homogene-
111 ously in the fast travelling fluid and are then deposited and cemented to the silica layer.
112 Through this work, we evaluate the first ever amorphous silica precipitation rates and mecha-
113 nisms inside in operando pipelines of an active geothermal power plant.

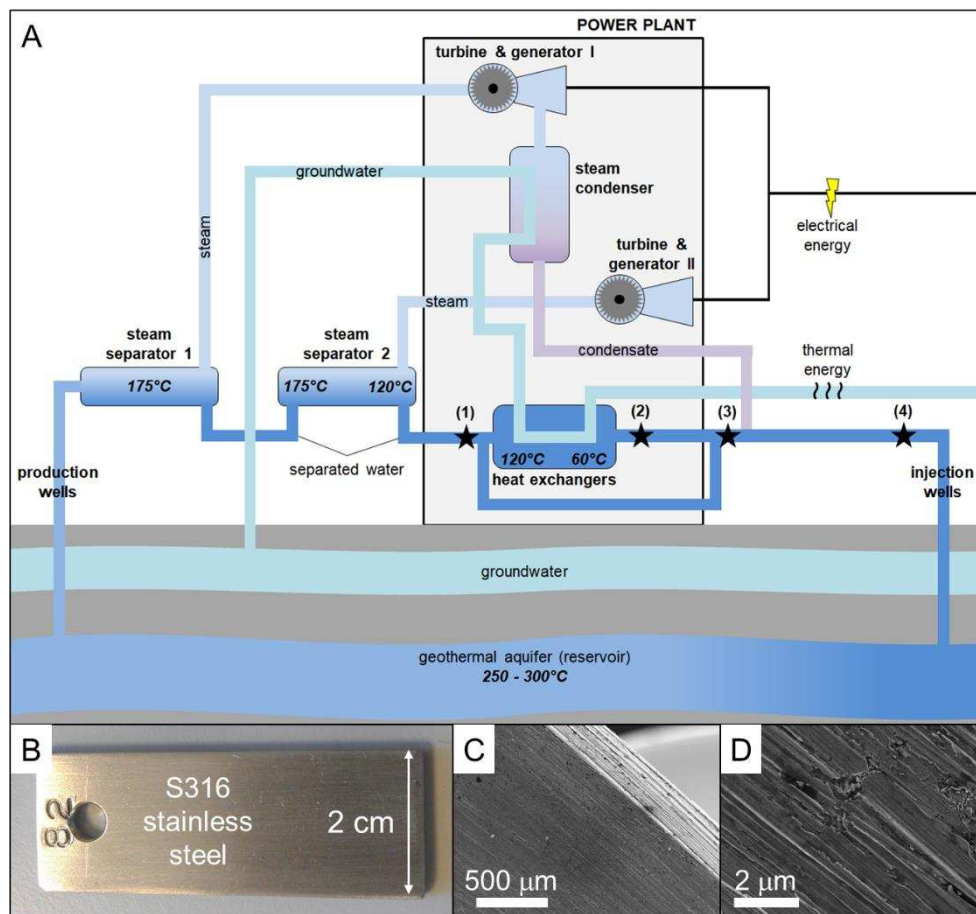
114

115 **2. Materials and methods**

116 **2.1 Field deployments**

117 The time-resolved deposition of amorphous silica was studied on stainless steel scaling plates
118 (5.4 x 2-2.5 cm) deployed for between 1 day and 10 weeks (Table 1) at four different locations
119 within the pipelines of the Hellisheiði power plant (Figure 1): (1) several metres before the heat
120 exchangers, (2) several metres after the heat exchangers, (3) several tens of metres downstream
121 of location 2, after a bypass with fluid that had not passed through the heat exchangers that
122 then re-joined the main pipeline and before mixing with condensed steam (equivalent to almost
123 pure water) and (4) ~ 1300 metres downstream from location 3, at the Húsmúli re-injection

124 site. These locations were chosen because they differed with respect to physicochemical con-
 125 ditions of the fluid (temperature, flow rate, silica concentration etc.) thus allowing us to study
 126 how these parameters affected silica precipitation. It is worth noting that due to operational
 127 constraints the time resolved deployments were not done in order of deployment length (Ta-
 128 ble 1).
 129



130
 131 Figure 1: System schematic of the Hellisheiði geothermal power plant (A) indicating the four
 132 sampling locations (stars) at which the scaling plates (B) were immersed. FEG-SEM images
 133 (C & D) showing the irregular texture of the steel surfaces before deployment.

134
 135 At each location, scaling plates made from S316 stainless steel (Figure 1 B – D) were
 136 attached to a sampling rod and inserted into the fast flowing geothermal fluid through valves

137 in the pipeline walls. The surfaces of the plates were aligned to be parallel to the flow. The
138 power plant operators monitor the temperatures and flow rates at each of the chosen sampling
139 locations hourly to identify changes in production parameters and as a guide for when mainte-
140 nance (e.g., heat exchanger cleaning) is required. These continuous datasets helped make sure
141 that the scaling plate deployments were started/finished during periods where no maintenance
142 was required. At the end of each deployment, the plates were removed from the fluid, gently
143 rinsed with distilled water to prevent the precipitation of salts during evaporation of the geo-
144 thermal fluid and then dried at 40 °C for up to 16 hours. For short deployments (1 day, 3 days
145 and 1 week), the scaling plates were weighted pre- and post-deployment in order to determine
146 the mass of precipitated silica. For deployments of 2 weeks or longer this was not considered
147 feasible as in most cases larger amounts of silica precipitated on the plates and some of the
148 accumulated silica would have been either lost because of the fast fluid flow rates (fluid flow
149 280 to 430 L/s) or during scaling plate handling post removal.

150 At the beginning and end of each deployment, the fluid at each location was sampled.
151 It was cooled down to ambient values (21 to 27 °C) using a ~ 5 m stainless steel coil and
152 temperature and pH were measured using a Metrohm Aquatrode plus pH electrode with a ther-
153 mocouple. Fluid samples were then collected into two Teflon gas sampling bulbs (300 mL,
154 rinsed 3x with separated water before use), assuring no air remained trapped within the bulbs.
155 These samples were used for analysis of dissolved CO₂ and H₂S. Subsequently a stainless steel
156 holder containing single-use 0.2 µm polycarbonate filter membranes (Whatman®) was used to
157 collect filtered fluid samples. These samples were divided into three different aliquots. For
158 cation analyses, aliquots were transferred into 120 mL into Nalgene bottles containing 2.5 mL
159 of ultrapure HNO₃ while for anions, 60 mL of the filtered geothermal fluid were transferred
160 into pre-cleaned Nalgene bottles. At selected time points, 5 mL of the filtered waters were in
161 addition transferred into Nalgene bottles containing 20 mL of MilliQ water for analysis of

162 monomeric silica contents. The dilution ensures that further polymerisation of silica is pre-
163 vented. After collection, the samples were stored at 3 – 6 °C for maximum 2 days before anal-
164 ysis of the dissolved gases and monomeric silica and for maximum 3 weeks for the analysis of
165 cations or anions. Finally, at locations 1 to 3, two litres of separated water were filtered through
166 ten pre-weighted 0.2 µm polycarbonate membranes to assess particles load, and separate
167 0.2 µm polycarbonate membranes were used to filter 100 mL to assess particle sizes, shapes
168 and distribution via electron microscopic imaging All membranes were dried at 40 °C for ~ 16
169 hours and re-weighed.

170

171 **2.2 Analyses of separated water**

172 Chloride was analysed by ion chromatography (IC) using a Thermoscientific Dionex system
173 DX600, equipped with a AG16 (2 x 5 mm) and AS16 (2 x 250 mm) column, with an analytical
174 uncertainty of ±5%, based on multiple standard measurements. The concentrations of the major
175 cations (Al, Ca, K, Na, Si) were analysed by inductively coupled plasma optical emission spec-
176 trometry (ICP-OES, Thermo Scientific iCAP7400; analytical uncertainty of < 4% based on
177 multiple standard measurements) while the trace cations (Mg, Fe) were analysed by inductively
178 coupled plasma mass spectrometry (ICP-MS, Thermo Scientific iCAPQc; analytical uncer-
179 tainty of < 3% based on multiple standard measurements).

180 The concentrations of dissolved CO₂ and H₂S were analysed by total alkalinity titration
181 (Metrohm 905 Titrando equipped with a Metrohm Aquatrode plus) and titration with mercury
182 acetate using dithizone as an indicator, respectively (Arnórsson et al., 2006). The analytical
183 uncertainties are ± 1% for total alkalinity titration and ± < 0.1 % for titration of H₂S. The
184 monomeric silica content was analysed based on the method described by Gunnarsson et al.
185 (2010) using a JENWAY 6300 spectrophotometer. In addition to total and monomeric silica,

186 “polymeric” silica was determined by subtracting the concentration of monomeric silica from
187 the total silica concentration ($< 0.2 \mu\text{m}$ filtered fraction).

188

189 **2.3 Analyses of precipitates on scaling plates and filter membranes**

190 The materials deposited on the scaling plates and filter membranes were analysed by field
191 emission gun scanning electron microscopy (FEG-SEM, FEI Quanta 650 at 15 keV, coated
192 with $\sim 40 \text{ nm}$ of gold). Selected, non-coated filter membranes were also imaged at ultra-high
193 resolution, using a low kV cold-field emission scanning electron microscope (CFE-SEM, Hi-
194 tachi SU8230 at 2 kV). The FEG-SEM images were used to determine the dimensions of the
195 observed structures by measuring widths and lengths of 70 to 100 structures or particles that
196 had formed or were deposited in the top side of each plate or filter manually.

197 The elemental composition of the precipitates was determined by energy dispersive
198 spectroscopy (EDS; AZtec software, Oxford Instruments, Version 2.2). From the scaling plates
199 onto which enough material had precipitated, material was scraped off and analysed by X-ray
200 diffraction (XRD; Bruker D8 diffractometer, $\text{CuK}\alpha_1$; $5 - 90^\circ 2\theta$; $0.01^\circ/\text{step}$; data evaluation by
201 the EVA software, Bruker, Version 3.0). XRD analyses of the materials on the filter mem-
202 branes was done with the filters glued directly onto the XRD silicon holders.

203 The internal structure, composition and thickness of the precipitates on the scaling
204 plates from location 1 were investigated via two approaches. For high resolution work, sections
205 ($15 \times 10 \times 0.15 \mu\text{m}$) were prepared by focused ion beam (FIB) milling at the German Research
206 Center for Geosciences (GFZ) Potsdam, Germany from the 1 day, 3 day and 1 week scaling
207 plates following the method described by Wirth (2009). The FIB foils were analysed using a
208 high-resolution transmission electron microscope (HR-TEM, TECNAI F20 X-Twin, 200 kV)
209 at GFZ equipped with a Gatan Tridiem Imaging Filter and an EDAX X-ray analyser. Secondly,
210 all scaling plates from location 1 (1 day to 10 weeks) were embedded in epoxy resin, cut along

211 the width of the scaling plates and polished before being imaged by FEG-SEM as described
212 above.

213

214 Table 1: Duration and starting/end dates of individual scaling plate deployments. The cleaning
215 of the heat exchangers in early October 2014 (after the 10 week and before the 2-week deploy-
216 ment) was part of regular (every 4 to 6 months) and scheduled maintenance at the Hellisheiði
217 power plant to remove the accumulated silica scales.

	Deployment [days]	Start date	End date
1 day	1	02/02/2015	03/02/2015
3 days	3	16/03/2015	19/03/2015
1 week	7	27/10/2014	03/11/2014
2 weeks	14	03/11/2014	17/11/2014
4 weeks	28	23/06/2014	21/07/2014
6 weeks	41	03/02/2015	16/03/2015
10 weeks	72	21/07/2014	01/10/2014
Cleaning of heat exchangers		06/10/2014	07/10/2014

218

219 **2.4 Geochemical simulations**

220 The composition of the separated waters as well as the measured pH and temperatures were
221 used as input parameters for geochemical simulations using PHREEQC (version 3.0, Parkhurst
222 and Appelo, 2013) with the phreeqc.dat database, updated with the thermodynamic data for
223 amorphous silica solubilities from Gunnarsson and Arnórsson (2000). Simulations were con-
224 ducted to derive the in-situ pH and Eh conditions and the saturation indices (SI) of the com-
225 pounds of interest in the geothermal fluid.

226

227 **2.5 Determination of precipitation rates**

228 The precipitation rates were evaluated via two approaches: (1) we quantified the amount of
229 material deposited on each plates (in mg) from the 1 day, 3 day and 1 week deployments at
230 each location and (2) we measured the average thickness of the precipitation layer for the 1-
231 week and longer deployments at location 1 only.

232 For the first approach, the precipitated amount was measured by weighting of the scaling
233 plates before and after the deployments and converted to a volume using a density of
234 $\rho_{\text{SiO}_2} = 2.25 \text{ mg/mm}^3$ for a high density vitreous silica scale (Mroczek et al., 2011). Assuming
235 that the layers were all made of silica and that they were of roughly constant thickness around
236 the plate, the thickness of the precipitates was calculated. We then used the mass of silica pre-
237 cipitated and the surface areas of the individual scaling plates to calculate precipitation rates.
238 Based on an average precipitation rate determined for the deployments up to 1 week, the thick-
239 ness of the precipitated silica layer was calculated from linear extrapolations for the longer
240 deployments. In order to evaluate the validity of such a linear extrapolation, the thickness of
241 silica layers on all plates from location 1 (from 1 to 10 weeks) were measured on the FIB
242 sections and the epoxy-embedded samples by HR-TEM and FEG-SEM respectively (as de-
243 scribed above). The thickness of each precipitated silica layer was measured at multiple loca-
244 tions around each plate ($n = 36$ to 113) to derive an average value. Using the same $\rho_{\text{SiO}_2} =$
245 2.25 mg/mm^3 , the mass of silica was calculated and converted to a precipitation rate.

246

247 **3. Results**

248 **3.1 Composition of separated water**

249 The four sampling locations differed with respect to fluid temperature, flow rate and fluid com-
250 position (Table 2). This was in a large part defined by their position within the Hellisheiði
251 geothermal power station (Figure 1). Location 1 (before the heat exchangers) was characterised

252 by fluids with temperatures of around 118 °C and a flow rate of nearly 420 L/s. The separated
253 water at this location was a low salinity NaCl fluid containing ~800 mg/L SiO₂, ~25 mg/L
254 CO_{2(aq)} and ~20 mg/L H₂S_(aq). The measured pH was 9.4, the calculated pH at the in situ tem-
255 perature was 8.5 and the Eh -0.56 V.

256 At location 2, after the separated water was cooled inside the heat exchanger (Figure
257 1), the fluid temperature was lower (~57 °C) but the flow rate and the fluid composition re-
258 mained identical to location 1. The measured/calculated pH was 9.4/9.0 and the calculated Eh
259 -0.46 V. These same conditions prevailed at location 3, further downstream from the heat ex-
260 changers (Figure 1) but the flow rate was much lower (~280 L/s) due to the differences in pipe
261 geometry. Just after location 3, steam condensate was added to the fluid (around 0.4 L of con-
262 densate per 1 L of separated water). The condensate was hotter than the separated water, thus
263 the temperature of the fluid at location 4 was higher (~73 °C). The addition of the condensate
264 downstream of location 3 and differences in pipe geometry resulted in the highest measured
265 flow rate (Table 2). The biggest effect of the mixing with condensate (= almost pure water)
266 was on the chemistry as it resulted in the concentrations of all fluid components and the pH
267 being lower at location 4.

268 The saturation index calculations revealed that the separated waters were supersaturated
269 with respect to amorphous silica at all locations (Table 3). The total silica reported in Table 2
270 represents the sum of all silica species: monomers (H₄SiO₄), oligomers/polymers (dimers, tri-
271 mers, tetramers etc.) and (nano)particulate silica < 0.2 µm. Partitioning the various silica spe-
272 cies reveals that in all cases monomeric silica was by far the dominant component (Table 3).
273 The proportion of monomeric silica decreased along the flow path from 85% down to 75%
274 from location 1 to 3. At the same time, the proportion of polymeric silica increased from 15 to
275 25% due to continuous polymerisation. At location 4, the dilution by the addition of steam
276 condensate caused the percentage of monomeric silica to increase to 86%.

277 Table 2: Average and standard deviation (as 1 SD) of temperature, fluid composition, pH, Eh
 278 and salinity as determined for the different fluid samples (n = 9) at each of the four sampling
 279 locations.

		Loc. 1	Loc. 2	Loc. 3	Loc. 4
Temperature	[°C]	117.8 ± 0.4	56.6 ± 1.6	58.0 ± 5.3	72.5 ± 11.2
Flow rate	[L/s]	416 ± 54	420 ± 51	282 ± 18	430 ± 29
SiO ₂	[mg/L]	802 ± 19	801 ± 30	794 ± 30	550 ± 76
Na	[mg/L]	204 ± 8	205 ± 9	207 ± 8	140 ± 10
Cl	[mg/L]	173 ± 12	171 ± 9	175 ± 6	120 ± 5
K	[mg/L]	34.7 ± 1.6	34.7 ± 1.7	35.1 ± 1.6	23.6 ± 1.2
CO ₂	[mg/L]	25.4 ± 5.5	25.2 ± 4.8	23.8 ± 3.7	18.5 ± 3.8
H ₂ S	[mg/L]	19.2 ± 2.9	19.8 ± 2.5	20.5 ± 1.9	14.3 ± 2.7
Al	[mg/L]	1.99 ± 0.09	2.04 ± 0.11	2.04 ± 0.11	1.36 ± 0.07
Ca	[mg/L]	0.71 ± 0.13	0.70 ± 0.06	0.71 ± 0.04	0.50 ± 0.06
Fe ¹⁾	[µg/L]	7.6 – 27.8	3.1 – 51.5	5.7 – 58.9	5.4 – 98.3
Mg ¹⁾	[µg/L]	3.2 – 70.1	<1.1 – 42.5	<1.1 – 42.2	1.4 – 52.4
pH meas. ²⁾		9.4 ± 0.2	9.4 ± 0.2	9.4 ± 0.2	9.1 ± 0.3
pH calc. ³⁾		8.5 ± 0.1	9.0 ± 0.1	9.0 ± 0.1	8.8 ± 0.2
Eh ³⁾	[V]	-0.56 ± 0.01	-0.46 ± 0.01	-0.47 ± 0.01	-0.48 ± 0.02
Salinity ⁴⁾	[%]	0.06	0.05	0.05	0.04

280 ¹⁾ The concentrations of Fe and Mg are reported as ranges rather than averages ± 1 SD due to the large variations
 281 in concentrations measured. These variations can stem from (a) corrosion of the steel pipes and redox effects for
 282 Fe and (b) precipitation of Fe- and Mg- containing aluminosilicates. These variations do not affect or change the
 283 silica precipitation and are thus not considered further.

284 ²⁾ As measured at 21 to 27 °C.

285 ³⁾ Derived from PHREEQC simulations at measured in situ temperatures and with the analysed fluid compositions.

286 ⁴⁾ Calculated based on the specific conductance derived from PHREEQC and the temperatures listed in this table.

287

288

289

290 Table 3: Silica speciation in the separated water at Hellisheiði

	Loc. 1	Loc. 2	Loc. 3	Loc. 4
SiO ₂ (total) [mg/L]	802 ± 19	801 ± 30	794 ± 30	550 ± 76
Solubility ¹⁾ [mg/L]	465	204	209	261
SI ²⁾ amorphous SiO ₂	0.10 ± 0.02	0.44 ± 0.02	0.42 ± 0.02	0.18 ± 0.08
Speciation [%]				
Monomeric ³⁾	85.0	81.4	75.5	85.8
“Polymeric” ⁴⁾	15.0	18.6	24.5	14.2
Particulate ⁵⁾	< 0.02	< 0.03	< 0.03	n/a
Particle sizes [µm] ⁶⁾				
on the filters mdn	0.2	0.1	0.1	n/a
IQR	(0.1 – 0.3)	(0.1 – 0.3)	(0.1 – 0.2)	
on the plates mdn	3.4	0.8	1.0	0.9
IQR	(1.7 – 6.8)	(0.4 – 1.7)	(0.4 – 1.7)	(0.5 – 3.1)

291 ¹⁾ Calculated based on Gunnarsson and Arnorsson (2000).

292 ²⁾ Saturation index, derived from PHREEQC simulations using the in-situ temperatures and with the fluid compositions given in Table 2.

293 ³⁾ Determined by analysing filtered (0.2 µm) and diluted sample aliquots using the spectrophotometric molybdate method.

294 ⁴⁾ Determined from subtracting the concentration of monomeric silica from the concentration of total silica (Table 2).

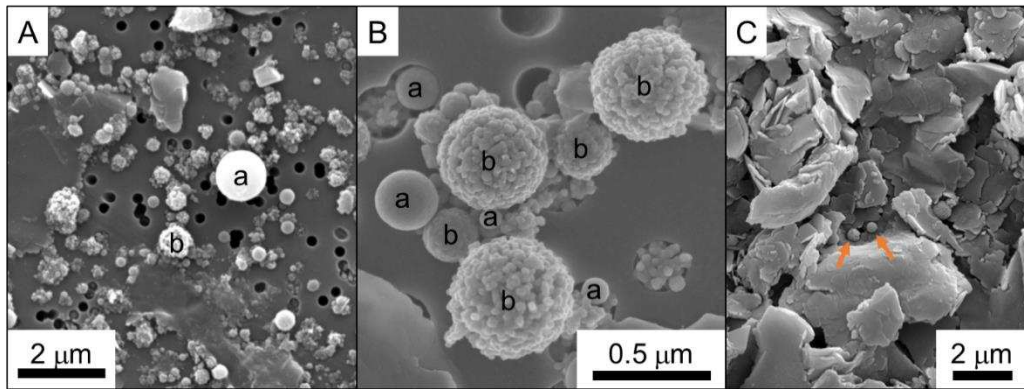
295 ⁵⁾ Determined from the weight difference of the 10 filter membranes before/after sampling and a density of 2.25 mg/mm³ for glass-like, high
296 density amorphous silica (Mroczek et al., 2011).

297 ⁶⁾ Determined from manual measurement of silica particles in FEG-SEM images found on filter membranes or scaling plates; mdn = median,
298 IQR = interquartile range (n = 70 to 100 particles per scaling plate or filter).

299

300 XRD analyses and imaging of the filter residues revealed that they consisted of amor-
301 phous silica particles. The proportion of particulate silica retained by the filter membranes, as
302 evaluated from the difference in weight of the filters, accounted for less than 0.05% of the total
303 silica (Table 3) at all locations. The particles on the filters had a mean diameter identical or
304 smaller than the pore sizes of the filter membranes (0.2 µm), yet particle sizes varied between
305 < 0.1 µm and in some exceptional cases over 20 µm. The particles could be subdivided into
306 two groups: (1) particles with a relatively smooth surface (Figure 2 A & B, marked a) and (2)

307 particles consisting of aggregates of much smaller and rougher surfaced particles (0.01 –
308 0.05 μm ; Figure 2 A & B, marked b). In addition, at locations 1 to 3, a few platy Al-Si contain-
309 ing phases were identified (Figure 2 A) by FEG-SEM EDS and confirmed as aluminosilicates,
310 specifically clinochlor by XRD. At location 4, silica particles were very rare and the abundance
311 of chlorite minerals such as chamosite and clinochlore and the magnesium silicate sepiolite
312 (identified by XRD, FEG-SEM EDS analyses and PHREEQC simulations) was high (Figure 2
313 C).
314



315
316 Figure 2: FEG-SEM images of 0.2 μm polycarbonate filter membranes with (A & B) two types
317 of silica particles (smooth particles marked a and rough particle aggregates marked b) from
318 location 1 and (C) platy aluminosilicates with very few and very small silica spheres (arrows)
319 from location 4.

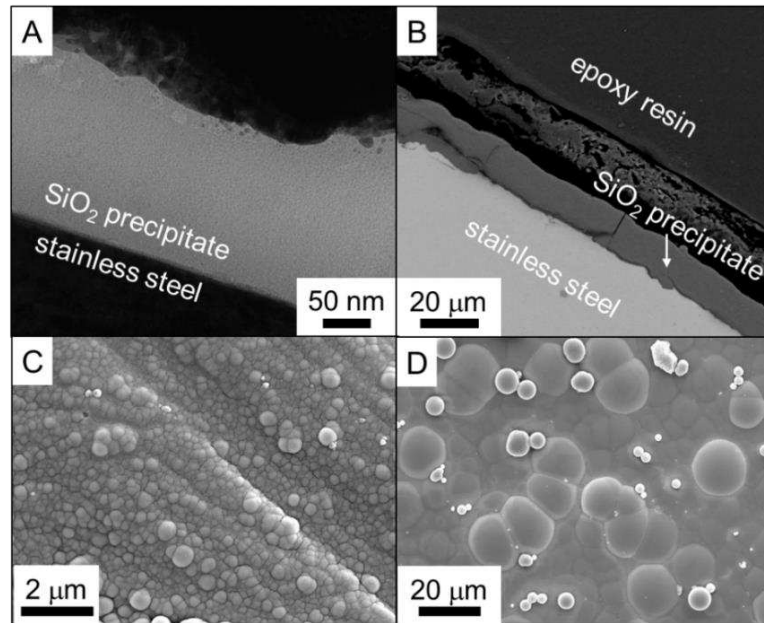
320

321 3.2 Composition and structure of precipitates on scaling plates

322 The majority of the precipitates on the deployed scaling plates were identified as amorphous
323 silica by XRD and EDS spot analyses. These amorphous silica precipitates were rarely inter-
324 spersed with other mineral and metal flakes, identified as aluminosilicates (based on FEG-SEM
325 EDS) and in some samples confirmed to be clinochlore (by XRD). In addition to these alu-
326 minosilicates, EDS analyses also revealed that the silica was not pure but most often peaks for

327 various ions from the geothermal fluid (Na, Cl, S, Al, Fe etc.) were observed associated with
328 the silica precipitates.

329



330

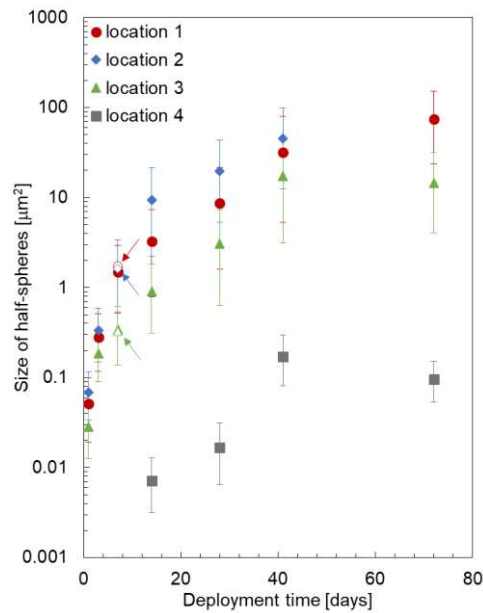
331 Figure 3: Electron microscope images showing a cross section of the precipitation layer after
332 (A) 1 day (FIB section imaged by TEM) and (B) 10 weeks (FEG-SEM image of a sample em-
333 bedded in epoxy resin, cut perpendicular to the plate). FEG-SEM images of the surface of
334 scaling plates deployed for (C) 1 day and (D) 10 weeks, respectively. All samples were from
335 location 1. Note the difference in scale.

336

337 The scaling plates were completely covered by a layer of amorphous silica, even after
338 just 1 day. This layer was very dense and it lacked any internal structure (Figure 3 A & B). The
339 average thickness of the silica layer was the same around each plate and no differences between
340 the individual faces of the plates (top vs. bottom, main face vs. edge) were observed. The layer
341 thickness increased over time; for example, it increased from 0.3 μm to > 20 μm over 10 weeks
342 on the plates deployed at location 1. The surface of the precipitation layer was uneven with a
343 botryoidal texture consisting of individual half-spheres (Figure 3 C & D) which grew in size

344 over time (Figure 4; evaluated through measurement of lengths and widths) but the number of
345 spheres decreased per area of plate.

346



347

348 Figure 4: Increase in the average area of the half-spheres over time at all four locations as
349 evaluated based on measured lengths and widths of between 70 and 100 half-spheres on each
350 plate. No 10-week sample was recovered at location 2. The empty symbols (highlighted by
351 arrows) represent the sizes of the half-spheres measured on the underside of the 1-week de-
352 ployment at locations 1 to 3. Note the logarithmic scale on the y-axis.

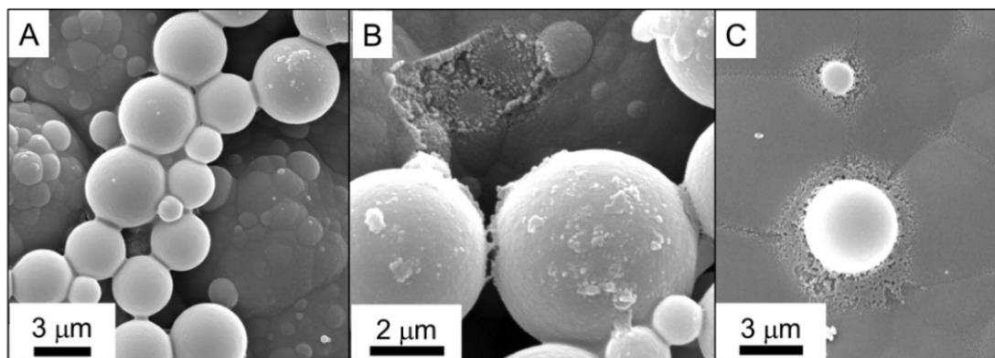
353

354 At all four locations rapid growth of the half-spheres during the 1 day to 2-week de-
355 ployments was followed by reduced growth rates for the longer deployments. The increase in
356 area of the half-spheres was fastest at locations 1 and 2, where the area of individual half-
357 spheres increased from $0.05 \mu\text{m}^2$ after 1 day to around $75 \mu\text{m}^2$ at 10 weeks. At location 3, the
358 growth was slower with the maximum area of half-spheres only reaching $15 \mu\text{m}^2$. Although
359 silica half-spheres were also observed at location 4, their growth was very slow and even after
360 10 weeks they only reached areas of $0.1 \mu\text{m}^2$. In all samples, measurements were carried out

361 on the top side of the scaling plates, yet for the 1 week deployment the areas of the half-spheres
362 were also measured on the bottom side of the scaling plates at all four locations to confirm that
363 the average areas on both sides were identical (open symbols in Figure 4).

364 In many cases, on top of the botryoidal silica layer, individual or merged silica particles
365 were observed (Figure 5). These spherical particles looked identical to the particles found on
366 the filters (Figure 2), but on average, they were markedly larger (Table 3). The spatial distri-
367 bution of the particles on the plates was completely random with some plates containing only
368 few particles, while other having larger areas covered by silica particles. In some instances,
369 neighbouring particles were cemented together (Figure 5 A) or to the surface of the existing
370 silica layer (Figure 5 B) by the deposition of dissolved silica. A very small number of these
371 individual silica particles became embedded into the botryoidal surface layer (Figure 5 C).

372



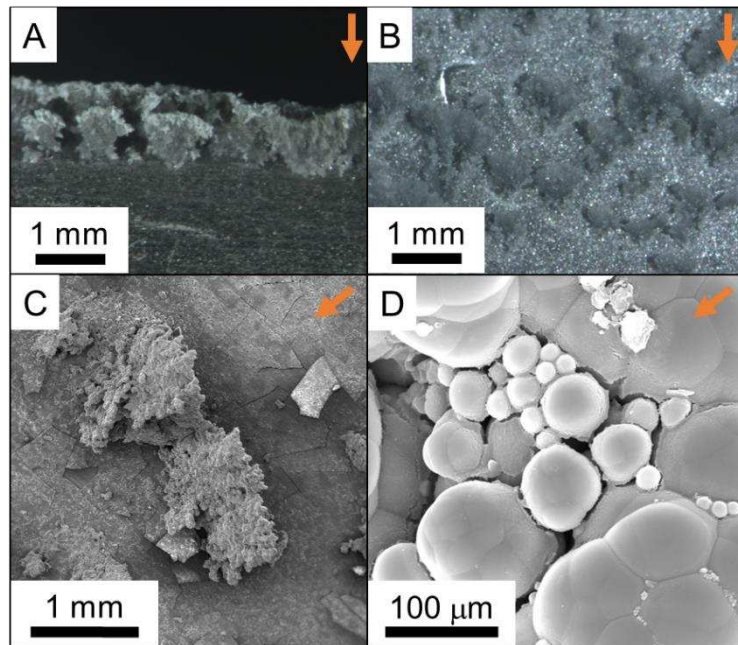
373

374 Figure 5: FEG-SEM images showing particles deposited onto the botryoidal silica layer where
375 they were (A) cemented together and/or (B) cemented to the surface or (C) (rarely) incorpo-
376 rated into the botryoidal silica layer. Images from locations 1 and 2.

377

378 Another mode of silica particle deposition was as 3D aggregates that had fan- to ridge-
379 shaped structures (Figure 6 A to C), pointing towards the direction of the flow and that were
380 cemented together (Figure 6 D). These microstructures were exclusively found on the top face
381 and along the plate edges oriented towards the flow in the 2-, 4- and 10-week deployments

382 (Figure 6 A). During the 2 week deployment at location 1, single fans reached a maximum of
383 300 μm in height. During the 4 week deployment, the fans grew to 700 μm in height (Figure 6
384 A) while on the 10 week scaling plate from this location, the fans had merged into ridges that
385 were up to 10 mm long and 1 mm high (Figure 6 B & C). At locations 2 and 3, fewer and
386 smaller fans (maximum 300 and 500 μm after 4 and 10 weeks, respectively; no fans after 2
387 weeks) were observed. Interestingly, during the 6-week deployment, independent of the loca-
388 tion, no 3D structures were observed to have grown on the ubiquitous botryoidal silica layer.
389



390
391 Figure 6: Microphotographs showing the 3D, fan-shaped structures found at location 1
392 following the 4- and 10-week deployments. Images (A) shows the edge of the plate and (B) the
393 surface of the plate. The fans (C) consisted of spherical silica aggregates that grew as a func-
394 tion of time seemingly by addition of individual particles that were then cemented together (D).
395 Flow direction indicated by arrows.
396

397 **4. Discussion**

398 **4.1 Precipitation pathways**

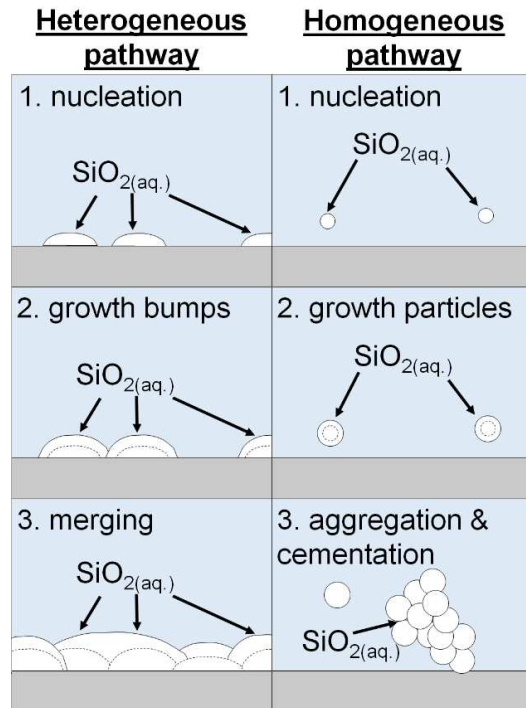
399 We observed two different silica textures on the scaling plates (Figure 3 and 6): dense silica
400 layers with a botryoidal surface and individual silica particles cemented into 3D structures.
401 While the silica layers were identified on all scaling plates and grew continuously in thickness,
402 the 3D structures were only observed during the 2, 4 and 10 week long deployments and never
403 at location 4, indicating that their formation was controlled by different processes and precipi-
404 tation pathways.

405 The botryoidal silica layers formed by heterogeneous nucleation and growth on/at the
406 steel-fluid-interface. All plates were made of the same non-polished S316 stainless steel (Fig-
407 ure 1 C &D) and in all cases botryoidal layers covered the steel surfaces completely, even
408 during the 1 day deployment. Thus, the plate surface properties were not a reason for the ob-
409 served differences in layer thickness (Figure 3) or size of half-spheres (Figure 4) between lo-
410 cations. These differences are a consequence of the changing silica precipitation depending on
411 local physicochemical conditions. The surface of the half-spheres appeared smooth (Figure 3)
412 and the scarcity of homogeneously formed particles (partly) embedded in the silica layer (Fig-
413 ure 5 C) suggests that the growth primarily occurred by addition of dissolved silica from the
414 fast flowing fluid, likely monomers. This is in line with results from previous studies
415 (Bohlmann et al., 1976; Bremere et al., 2000; Mroczek and McDowell, 1988), which suggested
416 that at neutral to slightly alkaline pH growth occurs primarily via monomeric silica addition
417 due to the negative surface charge of larger species and the resulting electrostatic repulsion.

418 The attachment of monomers to pre-existing silica surfaces follows the same mecha-
419 nism as silica polymerisation and growth is thus naturally enhanced when polymerisation rates
420 are high (i.e., at high total silica concentrations, high percentage of monomers, elevated
421 temperature and alkaline pH; Alexander et al., 1954; Bremere et al., 2000; Gunnarsson and

422 Arnórsson, 2005; Icopini et al., 2005; Weres et al., 1981). This explains why the growth rate
423 of the half-spheres is highest at location 1 (Figure 4). The fluid at location 1 had a high con-
424 centration of total silica (~800 ppm), a high percentage of silica monomers (85 %) as well as
425 the highest temperature (~120 °C), facilitating rapid attachment of monomeric silica from so-
426 lution onto the scaling plates. Location 2 shows identical total silica concentrations, but a some-
427 what lower monomeric silica content (81 %) and a lower temperature (~60 °C), explaining why
428 the growth of the half-spheres as a function of time is slower. At location 3 on the other hand,
429 the total silica content and fluid temperature were equal to location 2 but the fluid contained an
430 even lower percentage of silica monomers (~76 %) and thus an even slower growth of the half-
431 spheres. Finally, location 4 was characterised by the lowest growth rate for the half-spheres
432 (Figure 4). The fluid at this location was characterised by a higher temperature than at location
433 2 and 3 (~73 °C) and the highest monomer content (86 %) of all locations. However, the sub-
434 stantially lower total silica concentration (~550 ppm) was likely the reason for the much slower
435 growth rate, suggesting that the total silica concentration was the dominant factor in controlling
436 polymerisation rate of silica and thus attachment and growth of the half-spheres. This is in
437 agreement with previous studies (Gunnarsson and Arnórsson, 2005; Icopini et al., 2005; Weres
438 et al., 1981). The same studies also report a strong dependence of silica precipitation on pH.
439 However, the pH variation between the four locations in this study was only half a pH unit
440 (Table 2) and thus no marked effect of pH on silica precipitation was observed. The effect of
441 gravity was also investigated by not only measuring the half-spheres on the top sides of the
442 plates but also on the bottom sides (Figure 4). The half-spheres on both sides were identical at
443 all locations, indicating that gravity had no effect, an observation which is in line with hetero-
444 geneous nucleation and subsequent growth by monomer addition.

445



446

447 Figure 7: Schematic of the two silica precipitation pathways ($\text{SiO}_2(\text{aq})$ = silica monomers in
 448 solution) as they occur inside the pipelines of the Hellisheiði geothermal power plant.

449

450 The reduced growth of the silica half-spheres as a function of deployment time (Figure
 451 4) and the decrease in absolute numbers due to merging (Figures 3 C & D and Figure 7) is a
 452 consequence of preferential deposition of silica at half-sphere boundaries. Such intersections
 453 show an infinitely small negative radius of curvature and thus a solubility of zero (Iler, 1979).
 454 This relationship suggests that the growth of the silica layer was controlled by the rate of at-
 455 tachment of monomeric silica from the solution and not diffusion controlled, which is in line
 456 with previous studies (Bohlmann et al., 1980; Crerar et al., 1981; Weres et al., 1981).

457 The 3D structures on the other hand were composed of individual silica particles, which
 458 formed through homogeneous nucleation in the fluid. Once a nucleus formed, it grew by addi-
 459 tion of monomeric silica until it reached its optimal size (Figure 7). Homogeneous nucleation
 460 and particle growth were only controlled by the physicochemical conditions of the fluid. Under
 461 ambient conditions and up to 60 °C particles grow to ≤ 10 nm in laboratory experiments (Goto,

462 1956; Icopini et al., 2005; Iler, 1979; Tobler and Benning, 2013; Tobler et al., 2009). However,
463 at alkaline pH and in the absence of salts, particles can grow to sizes of 100 nm (Iler, 1979).
464 While this could explain the presence of the smallest particles observed on the filter membranes
465 (Figure 2 B), it does not explain the particles with diameters of several micrometres and smooth
466 surfaces (Figure 2 A). They likely formed due to the favourable conditions for growth inside
467 the pipelines (alkaline pH, elevated temperature, constant re-supply of dissolved silica and at
468 low salt concentrations) which are similar to the conditions in the industrial “build-up process”,
469 developed for the production of large particle silica sols (Morris and Vossos, 1970). In addition,
470 the fast flow rates inside the pipelines favour the transport of larger particles without deposi-
471 tion. However, these large particles only account for a small proportion of the total particulate
472 silica in the fluid. Nevertheless, they are of importance as they are preferentially deposited as
473 shown by the larger average particle size on the plates compared to the filters (Table 3). The
474 difference is most pronounced at location 1 and smaller at locations 2 and 3, indicating that the
475 particles grew larger at higher temperatures and/or that the fluid got depleted with respect to
476 large particles along the flow path, despite the high flow rate. Both factors also explain why
477 such particles were rare at location 4.

478 As the separated water also contained low concentrations of multivalent cations (Table
479 2), they potentially acted as flocculants between the negatively charged silica particles leading
480 to some particles becoming aggregated into larger particles (Figure 2 B) and the formation of
481 3D fan- and ridge-shaped structures (Figure 6) very similar to the dendritic precipitates pre-
482 dicted in hydrodynamic simulations (Hawkins et al., 2013; 2014). Within these 3D structures,
483 the individual particles were cemented together by monomeric silica from solution (Figure 6).
484 This occurred in the embayment between particles (Chigira and Watanabe, 1994; Rimstidt and
485 Cole, 1983), where the solubility of amorphous silica is zero due to the infinitely small negative
486 radius of curvature at the contact point (Iler, 1979). The 3D structures grew largest at location

487 1, likely due to the larger average size and higher number of particles, and were absent at loca-
488 tion 4 where there were only few silica particles in the fluid (Table 3). The 3D structures only
489 grew during the 2 week (only location 1), 4 week (locations 1 + 2) and 10 week (locations 1 –
490 3) deployments. This indicates that deployment time as well as particle numbers and/or sizes
491 (both highest at location 1) were the crucial factors controlling growth of these 3D structures.
492 Interestingly, the fan- and ridge-shaped structures were not observed during the 6-week de-
493 ployment. This was due to the much higher average flow rate of 516 L/s at locations 1 and 2
494 (compared to 416 L/s measured during the other deployments, Table 2) recorded during this
495 deployment. While the reason for this substantial increase in flow rate is unknown, it indicates
496 that a threshold flow rate exists, above which not enough particles are deposited for such 3D
497 structures to form.

498 Silica precipitates with morphologies similar to the botryoidal silica layers and 3D particle
499 aggregates described here for the Hellisheiði pipelines, were also described at other power
500 plants in Iceland and New Zealand (Brown and McDowell, 1983; Carroll et al., 1998;
501 Gudmundsson and Bott, 1979; Rothbaum et al., 1979; Thórhallsson et al., 1975), in silica sin-
502 ters from Iceland (Jones and Renaut, 2010) and in laboratory experiments mimicking the
503 growth of silica veins (Okamoto et al., 2010). This indicates that the silica precipitation mech-
504 anisms described here operate over a wide range of physicochemical conditions and different
505 geological settings.

506

507 **4.2 Quantification of precipitation rates**

508 The precipitation rates could only be determined for the heterogeneous pathway and the for-
509 mation of the botryoidal layer due to the strong dependency on flow rate and thus more erratic
510 deposition behaviour of the homogeneous pathway.

511 Initially, we determined the amount of silica deposited on the scaling plates by weight
512 up to the 1-week deployment. The amount increased four- to five-fold from 1 day to 1 week at
513 all locations (Table 4), yet the absolute mass deposited differed substantially between the four
514 locations. The total accumulated silica was highest at location 1 (13.2 mg) and slightly lower
515 at locations 2 (12.3 mg) and 3 (11.4 mg). Substantially less silica (3.2 mg) was deposited at
516 location 4 during the same time interval. As for the growth of the half-spheres (Figure 4), the
517 differences between the locations could be explained by changes in physicochemical conditions
518 affecting the attachment of dissolved silica from the fluid (i.e. silica concentration and mono-
519 mer content as well as temperature). The mass of silica deposited was used to calculate the
520 thickness of the formed silica layer and determine precipitation rates. The botryoidal silica
521 layers ranged from 1.7 to 2.4 μm at locations 1 to 3 and only 0.5 μm at location 4. The deter-
522 mined precipitation rates strongly decreased from the 1 day to the longer deployments (Table
523 4). This was due to the changing interactions controlling precipitation. Initially, deposition took
524 place at the steel-fluid interface and was controlled by the steel surface properties (e.g. rough-
525 ness) and the nucleation behaviour of silica. Once the surface was covered by silica nuclei,
526 which happened at some point during the first 24 hours of the deployments as evidenced by the
527 continuous botryoidal layer found on all plates deployed for 1 day, precipitation was controlled
528 by silica-silica interactions only. The precipitation rates determined for the 1-day deployments
529 (800 to over 1100 $\text{mg m}^{-2} \text{day}^{-1}$ at locations 1 to 3 and 315 $\text{mg m}^{-2} \text{day}^{-1}$ at location 4) were
530 strongly influenced by the interactions between silica and the steel plates and thus do not rep-
531 resent the long-term precipitation behaviour of silica from the fluid. Therefore, these rates were
532 not used to calculate an average precipitation rate for each location and linearly extrapolate the
533 thickness of the precipitation layer to 10 weeks (Figure 8 A). However, as with the evolution
534 of the size of the half-spheres (Figure 4), it was expected to see a decrease in growth of this

535 silica layer over time, meaning the extrapolation is representing a ‘worst case’ scenario rather
 536 than the behaviour of silica precipitation as a function of time.

537

538 Table 4: Thickness of the botryoidal silica layer based on the difference in pre- and post-de-
 539 ployment weights of scaling plates.

	Amount of silica precipitated		Thickness of layer [μm] ³⁾	Precipitation rate [$\text{mg m}^{-2} \text{day}^{-1}$] ⁴⁾
	[mg] ¹⁾	[mm^3] ²⁾		
Location 1				
1 day	2.5	1.1	0.5	1027
3 days	5.7	2.5	1.0	768
1 week	13.2	5.9	2.4	766
Location 2				
1 day	2.8	1.2	0.5	1124
3 days	5.6	2.5	1.0	756
1 week	12.3	5.5	2.2	717
Location 3				
1 day	2.0	0.9	0.4	803
3 days	5.8	2.6	1.0	783
1 week	11.4	5.1 ⁵⁾	1.7	663
Location 4				
1 day	0.8	0.3	0.1	315
3 days	0.6	0.3	0.1	82
1 week	3.2	1.4 ⁵⁾	0.5	189

540 ¹⁾ Calculated based on the weight difference of the scaling plate before and after deployment.

541 ²⁾ Calculated based on a density of 2.25 mg/mm^3 for glass-like, high density amorphous silica (Mroczek et al.,
 542 2011).

543 ³⁾ Calculated assuming a constant thickness of the silica layer around the whole plate.

544 ⁴⁾ Calculated using the amount precipitated and the surface area of the scaling plates. The average of the 3 day
 545 and 1 week rates was used for the extrapolation of the thickness of the silica layer to 10 weeks (Figure 8A).

546 ⁵⁾ Scaling plates 2.5 cm wide (all other scaling plates were 2 cm wide). Taken into account when calculating the
 547 thickness of the layer and the precipitation rate.

548 In order to better constrain the time-dependant deposition of silica, precipitation rates
549 up to 10 weeks were also determined at location 1 by measuring the thickness of the silica layer
550 using FIB sections and by imaging plates embedded in epoxy resin and cut perpendicularly.
551 The silica layer grew from 0.3 μm after 1 day to over 20 μm after 10 weeks (Table 5). The
552 values of the shorter deployments are in good agreement with the thicknesses calculated and
553 extrapolated based on the amount of silica. For the longer deployments (6 and 10 weeks), the
554 measured thickness was around 20% lower than the extrapolated value showing that the ex-
555 trapolation indeed represents a ‘worst case’ scenario (Figure 8B). The discrepancy is due to
556 the steadily decreasing precipitation rates (Table 5), which are not taken into account in the
557 linear extrapolation of the average precipitation rates. The decrease is caused by the disappear-
558 ance of preferential deposition sites (i.e. half-sphere boundaries) over time due to continuous
559 merging. This highlights the need for time-resolved and long-term studies (i.e. over weeks to
560 months) to determine reliable precipitation rates of silica inside in-use geothermal power
561 plants.

562 The above derived silica precipitation rates compare well with rates from other sites
563 where the physicochemical conditions of the fluids are similar. This includes the Sumikawa
564 power plant, Japan (Okazaki et al., 2017) and Ohaaki power station, New Zealand (Brown and
565 McDowell, 1983) where silica precipitation rates of around 840 and 1300 to 1800 $\text{mg m}^{-2} \text{day}^{-1}$
566 respectively were reported. However, care has to be taken to only compare processes, which
567 are indeed similar. Mroczek et al. (2017) for example also studied silica precipitation at Ohaaki
568 power station and reported much higher precipitation rates (up to 4500 $\text{mg m}^{-2} \text{day}^{-1}$), yet the
569 precipitates were described by the authors as “wavy silica spicules” and these seem more akin
570 to the 3D structures reported here, rather than the dense botryoidal layer from which we deter-
571 mined our precipitation rates. It is thus likely that the rates determined by Mroczek et al. rep-
572 resent the deposition rate of silica particles rather than silica precipitation via the heterogeneous

573 pathway and cannot therefore be compared directly to the rates reported in this study. Care is
574 also needed when comparing different precipitation settings. Several studies reported silica
575 precipitation rates from in situ sinter growth experiments around hot springs or geothermal
576 wastewater drains (Handley et al., 2005; Mountain et al., 2003; Tobler et al., 2008). The rates
577 reported in these studies are generally higher than the ones reported for silica scaling inside
578 geothermal power plants. For example, the rates reported from Krafla (Tobler et al., 2008)
579 under physicochemical conditions comparable to the separated water studied here, are more
580 than 50 times higher. This is because subaerial silica sinter formation occurs predominantly at
581 the air-water interface where recurring wetting-evaporation cycles occur as well as other hy-
582 drodynamic processes including wave action, capillary action, diffusion and splash which en-
583 hance silica precipitation. In addition, the presence of microbes and biofilms also accelerates
584 silica precipitation and thus increases the deposition rates compared with purely abiotic pre-
585 cipitation. The factors affecting silica precipitation most strongly are therefore vastly different
586 in these settings compared to geothermal pipelines.

587

588 **4.3 Implications on predicting silica scaling**

589 Based on the growth of the half-spheres (Figure 4) and the determined amounts of silica pre-
590 cipitated in this study (Tables 4 and 5) we can conclude that silica precipitation was fastest at
591 locations 1 and 2 and slowest at location 4. This is in conflict with the saturation indices (SIs)
592 calculated by PHREEQC (Table 3), which suggested that precipitation should be fastest at lo-
593 cations 2 and 3 (highest SIs = highest driving force for precipitation). However, the SI is a
594 purely thermodynamic concept, which is only of limited use in a system as dynamic as a geo-
595 thermal power plant where changes in the physicochemical conditions (e.g., cooling in the heat
596 exchangers, dilution by steam condensate) occur rapidly and over short distances due to the
597 fast flow rates. Therefore, it is also not surprising that our precipitation rates do not agree with

598 theoretical calculations based on Rimstidt and Barnes (1980), which, when taking into account
 599 our solution composition and saturation indices derived from PHREEQC, yielded theoretical
 600 precipitation rates of 0.35 to 0.75 mg m⁻² day⁻¹. However, even if we were to take kinetics into
 601 account to simulate the precipitation, the accuracy of our extrapolation predictions would likely
 602 not improve as the kinetics of silica polymerisation and silica (nano)particle formation are still
 603 highly contentious (reviewed by Tobler et al., 2017). This lack of predictability is a major issue
 604 in the development of geothermal resources as it is commonly cheaper and easier to keep the
 605 fluid at temperatures high enough to prevent silica supersaturation rather than to mitigate sub-
 606 stantial silica scaling during operation.

607

608 Table 5: Thickness of the precipitated silica layer at location 1 from FIB sections and samples
 609 embedded in epoxy as well as calculated precipitation rates.

	Measured [μm]		Amount of silica [mg] ¹⁾	Precipitation rate [$\text{mg m}^{-2} \text{day}^{-1}$] ²⁾
	FIB sections	Embedded		
1 day	0.3	-	1.7	675
3 days	1.5	-	8.3	1125
1 week	3.0	2.6	16.6 / 14.4	965 / 836
2 weeks	-	4.5	24.9	725
4 weeks	-	9.6	53.2	773
6 weeks	-	12.2	67.4	669
10 weeks	-	20.2	111.7	632

610 ¹⁾ Calculated based on a density of 2.25 mg/mm³ for glass-like, high density amorphous silica (Mroczek et al.,
 611 2011) and the volume of silica precipitated assuming a constant thickness of the precipitation layer all around the
 612 scaling plates.

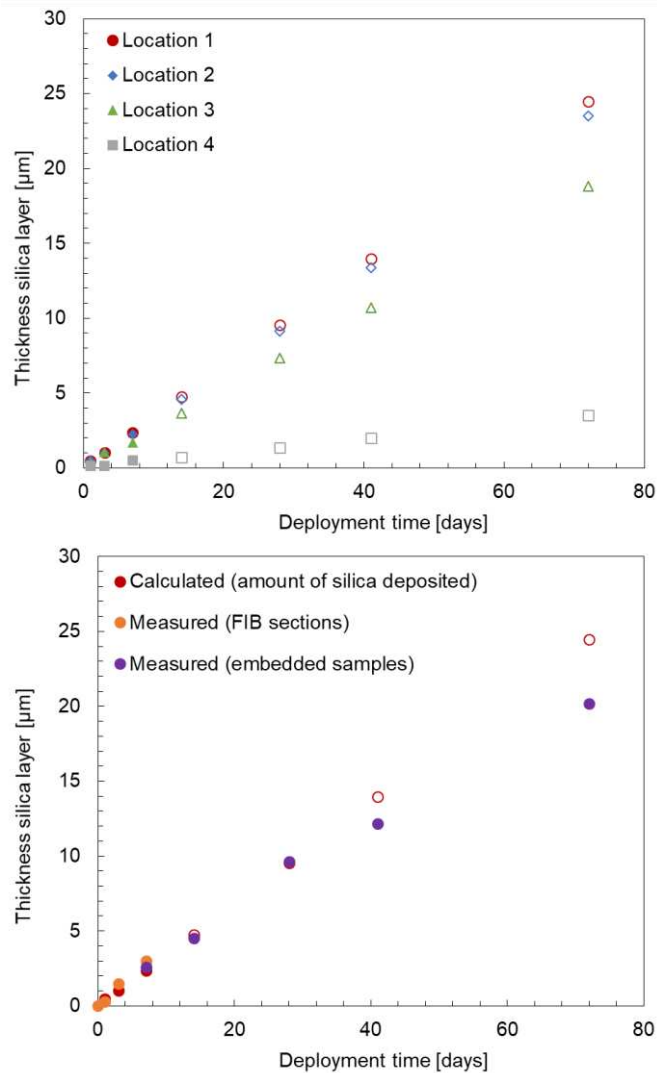
613 ²⁾ Calculated using the amount precipitated and the surface area of the scaling plates.

614

615 **5 Summary**

616 In this study, we evaluated for the first time silica precipitation rates and mechanisms inside
617 pipelines of an in-work high-entropy geothermal power station in a time resolved manner,
618 showing how a well-constrained geothermal power plant is a perfect study site for mineral
619 precipitation. Our results documented that amorphous silica precipitates via two pathways at
620 Hellisheiði: (1) rapid heterogeneous nucleation of silica on any exposed surface resulting in
621 half-spheres which, by addition of monomeric silica from solution, grow into a botryoidal silica
622 layer and (2) homogeneous nucleation of nano- and micro-particles in the fast flowing fluid,
623 followed by their growth and deposition on the pre-existing botryoidal layers leading to 3D
624 fan- and ridge-shaped structures. Both pathways are predominantly controlled by total silica
625 concentration, silica monomer content and temperature, while particle deposition is also
626 strongly affected by hydrodynamics. Observations from other geothermal systems suggest that
627 these precipitation modes are not unique to Hellisheiði but occur over a wide range of different
628 conditions.

629



630

631 Figure 8: Increasing thickness of the botryoidal silica layer over time: (A) calculated from
 632 the weight of silica and a density of 2.25 mg/mm^3 (Mroczek et al., 2011) at all locations up to
 633 1 week (solid symbols) and linear extrapolations up to 10 weeks (empty symbols) and (B) de-
 634 rived from the weight of the scaling plates pre- and post-deployment (red) as well as thick-
 635 ness measurements from FIB sections (orange) and embedded samples (purple) by electron
 636 microscopy at location 1.

637

638 **Acknowledgments**

639 This research was made possible by Marie Curie grants from the European Commission in
 640 the framework of the MINSC Initial Training Research network [Project number 290040] to

641 Liane G. Benning and Caroline L. Peacock and the framework of the NanoSiAl Individual
642 Fellowship [Project No. 703015] to Tomasz Stawski. Daniela B. van den Heuvel acknowl-
643 edges financial support by the International Geothermal Association (IGA) in the framework
644 of the 2014 PhD Student Grant. Tomasz Stawski and Liane G. Benning also acknowledge the
645 financial support of the Helmholtz Recruiting Initiative. We thank T. Windross and S. Bur-
646 gess for preparation of all scaling plates and H. Bergmann for his help with the deployments
647 at Hellisheiði power plant. We are grateful for the fluid analyses done at Reykjavik Energy
648 and by S. Reid and F. Keay at the University of Leeds. We thank A. Schreiber and R. Wirth
649 at the GFZ Potsdam for preparation of FIB foils and subsequent analyses by TEM. We also
650 acknowledge analytical support by L. Neve (XRD) and R. Walshaw (SEM), both University
651 of Leeds. We would like to thank H. Williams (University of Leeds), Th. Aebi and N. Lö-
652 tscher (both University of Bern) for help with embedding of the samples in resin and the sub-
653 sequent cutting and polishing.

654

655 References

656

- 657 Alexander, G.B., Heston, W. and Iler, R. (1954) The solubility of amorphous silica in water.
658 *The Journal of Physical Chemistry* 58, 453-455.
- 659 Arnórsson, S. (1975) Application of the silica geothermometer in low temperature
660 hydrothermal areas in Iceland. *American Journal of Science* 275.
- 661 Arnórsson, S., Bjarnason, J.Ö., Giroud, N., Gunnarsson, I. and Stefánsson, A. (2006) Sampling
662 and analysis of geothermal fluids. *Geofluids* 6, 203-216.
- 663 Benning, L.G. and Waychunas, G.A. (2007) Nucleation, growth, and aggregation of mineral
664 phases: Mechanisms and kinetic controls, *Kinetics of Water-Rock Interaction*. Springer, pp.
665 259-333.
- 666 Bohlmann, E., Shor, A. and Berlinski, P. (1976) Precipitation and scaling in dynamic
667 geothermal systems. Oak Ridge National Laboratories, p. 21680.
- 668 Bohlmann, E.G., Mesmer, R.E. and Berlinski, P. (1980) Kinetics of silica deposition from
669 simulated geothermal brines. *Society of Petroleum Engineers Journal* 20, 239-248.

670 Braunstein, D. and Lowe, D.R. (2001) Relationship between spring and geyser activity and the
671 deposition and morphology of high temperature (> 73 C) siliceous sinter, Yellowstone National
672 Park, Wyoming, USA. *Journal of Sedimentary Research* 71, 747-763.

673 Bremere, I., Kennedy, M., Mhyio, S., Jaljuli, A., Witkamp, G.-J. and Schippers, J. (2000)
674 Prevention of silica scale in membrane systems: removal of monomer and polymer silica.
675 *Desalination* 132, 89-100.

676 Brown, K. and McDowell, G. (1983) pH control of silica scaling, *Proceedings of the 5th New
677 Zealand Geothermal Workshop, New Zealand*, pp. 157-161.

678 Cady, S. and Farmer, J. (1996) Fossilization processes in siliceous thermal springs: trends in
679 preservation along thermal gradients. *Evolution of hydrothermal ecosystems on Earth (and
680 Mars*, 150-173.

681 Carroll, S., Mroczek, E., Alai, M. and Ebert, M. (1998) Amorphous silica precipitation (60 to
682 120 C): Comparison of laboratory and field rates. *Geochimica et Cosmochimica Acta* 62, 1379-
683 1396.

684 Chigira, M. and Watanabe, M. (1994) Silica precipitation behavior in a flow field with negative
685 temperature gradients. *Journal of Geophysical Research: Solid Earth* 99, 15539-15548.

686 Crerar, D.A., Axtmann, E.V. and Axtmann, R.C. (1981) Growth and ripening of silica
687 polymers in aqueous solutions. *Geochimica et Cosmochimica Acta* 45, 1259-1266.

688 Dixit, C., Bernard, M.-L., Sanjuan, B., André, L. and Gaspard, S. (2016) Experimental study
689 on the kinetics of silica polymerization during cooling of the Bouillante geothermal fluid
690 (Guadeloupe, French West Indies). *Chemical Geology* 442, 97-112.

691 Dugger, D.L., Stanton, J.H., Irby, B.N., McConnell, B.L., Cummings, W.W. and Maatman,
692 R.W. (1964) The Exchange of Twenty Metal Ions with the Weakly Acidic Silanol Group of
693 Silica Gell, 2. *The Journal of Physical Chemistry* 68, 757-760.

694 Fleming, B. and Crerar, D. (1982) Silicic acid ionization and calculation of silica solubility at
695 elevated temperature and pH application to geothermal fluid processing and reinjection.
696 *Geothermics* 11, 15-29.

697 Fleming, B.A. (1986) Kinetics of reaction between silicic acid and amorphous silica surfaces
698 in NaCl solutions. *Journal of Colloid and Interface Science* 110, 40-64.

699 Fournier, R. and Rowe, J. (1966) Estimation of underground temperatures from the silica
700 content of water from hot springs and wet-steam wells. *American Journal of Science* 264, 685-
701 697.

702 Gallup, D.L. (1997) Aluminum silicate scale formation and inhibition: scale characterization
703 and laboratory experiments. *Geothermics* 26, 483-499.

704 Goto, K. (1956) Effect of pH on polymerization of silicic acid. *The Journal of Physical
705 Chemistry* 60, 1007-1008.

706 Gudmundsson, J.S. and Bott, T.R. (1979) Deposition of silica from geothermal waters on heat
707 transfer surfaces. *Desalination* 28, 125-145.

708 Gunnarsson, I. and Arnórsson, S. (2000) Amorphous silica solubility and the thermodynamic
709 properties of H₄SiO₄ in the range of 0 to 350 C at P_{sat}. *Geochimica et Cosmochimica Acta* 64,
710 2295-2307.

- 711 Gunnarsson, I. and Arnórsson, S. (2003) Silica scaling: The main obstacle in efficient use of
712 high-temperature geothermal fluids, Proceedings International Geothermal Conference,
713 Reykjavik, pp. 30-36.
- 714 Gunnarsson, I. and Arnórsson, S. (2005) Impact of silica scaling on the efficiency of heat
715 extraction from high-temperature geothermal fluids. *Geothermics* 34, 320-329.
- 716 Gunnarsson, I., Ívarsson, G., Sigfússon, B., Thrastarson, E.Ö. and Gíslason, G. (2010)
717 Reducing silica deposition potential in waste waters from Nesjavellir and Hellisheiði Power
718 Plants, Iceland, Proceedings World Geothermal Congress, Bali.
- 719 Hair, M.L. and Hertl, W. (1970) Acidity of surface hydroxyl groups. *The Journal of Physical*
720 *Chemistry* 74, 91-94.
- 721 Handley, K., Campbell, K., Mountain, B. and Browne, P. (2005) Abiotic–biotic controls on the
722 origin and development of spicular sinter: in situ growth experiments, Champagne Pool,
723 Waiotapu, New Zealand. *Geobiology* 3, 93-114.
- 724 Harrar, J., Locke, F., Otto Jr, C., Lorensen, L., Monaco, S. and Frey, W. (1982) Field tests of
725 organic additives for scale control at the Salton Sea geothermal field. *Society of Petroleum*
726 *Engineers Journal* 22, 17-27.
- 727 Hawkins, C., Angheluta, L., Hammer, Ø. and Jamtveit, B. (2013) Precipitation dendrites in
728 channel flow. *Europhysics Letters* 102, 54001.
- 729 Hawkins, C., Angheluta, L. and Jamtveit, B. (2014) Hydrodynamic shadowing effect during
730 precipitation of dendrites in channel flow. *Physical Review E* 89, 022402.
- 731 Icopini, G.A., Brantley, S.L. and Heaney, P.J. (2005) Kinetics of silica oligomerization and
732 nanocolloid formation as a function of pH and ionic strength at 25 C. *Geochimica et*
733 *Cosmochimica Acta* 69, 293-303.
- 734 Iler, R.K. (1979) *The chemistry of silica: solubility, polymerization, colloid and surface pro*
735 *perties, and biochemistry*. Wiley, London.
- 736 Jones, B. and Renaut, R.W. (2004) Water content of opal-A: implications for the origin of
737 laminae in geysirite and sinter. *Journal of Sedimentary Research* 74, 117-128.
- 738 Jones, B. and Renaut, R.W. (2010) Impact of seasonal changes on the formation and
739 accumulation of soft siliceous sediments on the discharge apron of Geysir, Iceland. *Journal of*
740 *Sedimentary Research* 80, 17-35.
- 741 Kitahara, S. (1960) The polymerization of silicic acid obtained by the hydrothermal treatment
742 of quartz and the solubility of amorphous silica. *Review of Physical Chemistry Japan* 30, 131-
743 137.
- 744 Konhauser, K.O., Jones, B., Phoenix, V.R., Ferris, G. and Renaut, R.W. (2004) The microbial
745 role in hot spring silicification. *AMBIO: A Journal of the Human Environment* 33, 552-558.
- 746 Konhauser, K.O., Phoenix, V.R., Bottrell, S.H., Adams, D.G. and Head, I.M. (2001)
747 Microbial–silica interactions in Icelandic hot spring sinter: possible analogues for some
748 Precambrian siliceous stromatolites. *Sedimentology* 48, 415-433.
- 749 Meier, D., Gunnlaugsson, E., Gunnarsson, I., Jamtveit, B., Peacock, C. and Benning, L. (2014)
750 Microstructural and chemical variation in silica-rich precipitates at the Hellisheiði geothermal
751 power plant. *Mineralogical Magazine* 78, 1381-1389.
- 752 Morris, M. and Vossos, P.H. (1970) Large particle silica sols and method of production. Google
753 Patents.

754 Mountain, B., Benning, L. and Boerema, J. (2003) Experimental studies on New Zealand hot
755 spring sinters: rates of growth and textural development. *Canadian Journal of Earth Sciences*
756 40, 1643-1667.

757 Mroczek, E., Graham, D. and Bacon, L. (2011) Silica deposition experiments: past work and
758 future research directions, *Proceedings International Workshop on Mineral Scaling in*
759 *Geothermal Environments*, Manila.

760 Mroczek, E., Graham, D., Siega, C. and Bacon, L. (2017) Silica scaling in cooled silica
761 saturated geothermal water: Comparison between Wairakei and Ohaaki geothermal fields, New
762 Zealand. *Geothermics* 69, 145-152.

763 Mroczek, E. and McDowell, G. (1988) Silica scaling field experiments, *New Zealand*
764 *Geothermal Workshop*, Auckland.

765 Noguera, C., Fritz, B. and Clément, A. (2015) Precipitation mechanism of amorphous silica
766 nanoparticles: a simulation approach. *Journal of Colloid and Interface Science* 448, 553-563.

767 Okamoto, A., Saishu, H., Hirano, N. and Tsuchiya, N. (2010) Mineralogical and textural
768 variation of silica minerals in hydrothermal flow-through experiments: Implications for quartz
769 vein formation. *Geochimica et Cosmochimica Acta* 74, 3692-3706.

770 Okazaki, T., Orii, T., Ueda, A., Ozawa, A. and Kuramitz, H. (2017) Fiber Optic Sensor for
771 Real-Time Sensing of Silica Scale Formation in Geothermal Water. *Scientific Reports* 7.

772 Padilla, S.R.M., Barnett, P., Castro, M., Guerra, E. and Henríquez, J.L. (2005) Silica
773 Polymerization and Deposition Trials at the Berlin Geothermal Field, El Salvador, *Proceedings*
774 *World Geothermal Congress*.

775 Parkhurst, D.L. and Appelo, C. (2013) Description of input and examples for PHREEQC
776 version 3: a computer program for speciation, batch-reaction, one-dimensional transport, and
777 inverse geochemical calculations. US Geological Survey.

778 Preston, L., Benedix, G., Genge, M. and Sephton, M. (2008) A multidisciplinary study of silica
779 sinter deposits with applications to silica identification and detection of fossil life on Mars.
780 *Icarus* 198, 331-350.

781 Rimstidt, J. and Cole, D. (1983) Geothermal mineralization. I. The mechanism of formation of
782 the Beowawe, Nevada, Siliceous sinter deposit. *Am. J. Sci.:(United States)* 283.

783 Rimstidt, J.D. and Barnes, H. (1980) The kinetics of silica-water reactions. *Geochimica et*
784 *Cosmochimica Acta* 44, 1683-1699.

785 Rothbaum, H., Anderton, B., Harrison, R., Rohde, A. and Slatter, A. (1979) Effect of silica
786 polymerisation and pH on geothermal scaling. *Geothermics* 8, 1-20.

787 Seward, T. (1974) Determination of the first ionization constant of silicic acid from quartz
788 solubility in borate buffer solutions to 350 C. *Geochimica et Cosmochimica Acta* 38, 1651-
789 1664.

790 Thórhallsson, S., Ragnars, K., Arnórsson, S. and Kristmannsdóttir, H. (1975) Rapid scaling of
791 silica in two district heating systems, *United Nations Symposium on the Development and Use*
792 *of Geothermal Resources*, San Fransico, pp. 1445-1449.

793 Tobler, D.J. and Benning, L.G. (2013) In-situ and time resolved nucleation and growth of silica
794 nanoparticles forming under simulated geothermal conditions. *Geochimica et Cosmochimica*
795 *Acta* 114, 156-168.

- 796 Tobler, D.J., Shaw, S. and Benning, L.G. (2009) Quantification of initial steps of nucleation
797 and growth of silica nanoparticles: An in-situ SAXS and DLS study. *Geochimica et*
798 *Cosmochimica Acta* 73, 5377-5393.
- 799 Tobler, D.J., Stawski, T.M. and Benning, L.G. (2017) Silica and alumina nanophases: natural
800 processes and industrial applications, *New Perspectives on Mineral Nucleation and Growth*.
801 Springer, pp. 293-316.
- 802 Tobler, D.J., Stefansson, A. and Benning, L.G. (2008) *In-situ* grown silica sinters in Icelandic
803 geothermal areas. *Geobiology* 6, 481-502.
- 804 Weres, O., Yee, A. and Tsao, L. (1981) Kinetics of silica polymerization. *Journal of Colloid*
805 *and Interface Science* 84, 379-402.
- 806 Wirth, R. (2009) Focused Ion Beam (FIB) combined with SEM and TEM: Advanced analytical
807 tools for studies of chemical composition, microstructure and crystal structure in geomaterials
808 on a nanometre scale. *Chemical Geology* 261, 217-229.
- 809 Yokoyama, T., Sato, Y., Maeda, Y., Tarutani, T. and Itoi, R. (1993) Siliceous deposits formed
810 from geothermal water I. The major constituents and the existing states of iron and aluminium.
811 *Geochemical Journal* 27, 375-384.
- 812